Hugoniot, sound speed, and phase transitions of single-crystal sapphire for pressures 0.2–2.1 TPa

Chad A. McCoy, Pat Kalita, Marcus D. Knudson, Michael P. Desjarlais, Sakun Duwal, and Seth Root

Phys. Rev. B **107**, 214102 — Published 15 June 2023

DOI: 10.1103/PhysRevB.107.214102

Hugoniot, sound speed, and phase transitions of single-crystal sapphire for pressures 0.2-2.1 TPa

Chad A. McCoy, Pat Kalita, Marcus D. Knudson, Michael P. Desjarlais, Sakun Duwal, and Seth Root
Sandia National Laboratories, Albuquerque, NM 87185

Sapphire (Al_2O_3) is a major constituent of the Earth's mantle and has significant contributions to the field of high-pressure physics. Constraining its Hugoniot over a wide pressure range and identifying the location of shock-driven phase transitions allows for development of a multiphase equation of state and enables its use as an impedance-matching standard in shock physics experiments. Here we present measurements of the principal Hugoniot and sound velocity from direct impact experiments using magnetically-launched flyers on the Z machine at Sandia National Laboratories. The Hugoniot was constrained for pressures from 0.2-2.1 TPa and a four-segment piecewise linear shock velocity – particle velocity fit was determined. First-principles molecular dynamics simulations were conducted and agree well with the experimental Hugoniot. Sound speed measurements identified the onset of melt between 450 and 530 GPa, and the Hugoniot fit refined the onset to 525±13 GPa. A phase diagram which incorporates literature DAC data and melting measurements is presented.

Introduction

Sapphire (Al_2O_3) is an important material in high-pressure physics. It has been used as a window in shock experiments,[1, 2] pressure standard (as ruby in diamond anvil cell (DAC) experiments,[3] and cell material for reverberating shock[4] and precompressed shock[5] experiments. However, the properties of sapphire are poorly known for pressures >350 GPa, and the pressure at which shock melting occurs has only recently been identified.[6] Measuring its Hugoniot in the liquid phase and constructing a multiphase equation of state (EOS) will enable its use as a window for future experiments at extreme pressure.

In addition to its use in high-pressure physics, sapphire is of interest to geophysics as an end-member of the Earth's mantle.[7] In solid solution with $MgSiO_3$ garnet, perovskite, and post-perovskite, the presence of Al_2O_3 changes the physical and thermodynamic properties of the pure phases and affects spin states of iron impurities in the system.[8, 9]

At static high pressures, two phase transitions have been experimentally observed in Al_2O_3: from corundum to Rh_2O_3-type at 80-110 GPa,[10-13] and from Rh_2O_3-type to $CaIrO_3$-type at 130-170 GPa.[11, 12] The transition from corundum to Rh_2O_3-type has also been identified from dynamic experiments at ~80 GPa[14] and diffraction measurements later confirmed the phase at 107 GPa.[15] First-principles calculations have predicted an additional phase transition along the Hugoniot from the $CaIrO_3$-type to a U_2S_3-type at 370-400 GPa.[16, 17] This phase has not been identified experimentally, and limited shock data exists at higher pressure. The melt curve of sapphire has been measured in a diamond anvil cell to ~30 GPa[18] and calculated to ~150 GPa.[19] Simon fits to molecular dynamics simulations have estimated the principal Hugoniot to intersect the melt curve between 400 and 550 GPa.[20] Recent measurements of the shock temperature using explosive lenses were used to determine melting at ~500 GPa and ~11000K.[6]

The Hugoniot of single-crystal sapphire has previously been measured with high precision up to 340 GPa using explosively-driven shocks[21, 22] and gas-gun launched impactors.[14, 23-25] Three additional Hugoniot data at pressures up to 1.9 TPa have been measured using laser-driven shocks, however the uncertainty in that data is large.[20] Explosively-driven Hugoniot measurements at pressures up to 1.3 TPa have been reported recently, but the scatter in the results precludes adequate constraint of the EOS.[6] At low (<20

GPa) pressures, the Hugoniot and optical properties have been extensively studied, and sapphire is commonly used as a shock window for experiments in this regime.[1, 2, 22, 25, 26] The strength of sapphire has also been investigated under shock compression on gas gun and laser facilities.[15, 22, 24, 25, 27]

Magnetically-accelerated flyer plates on the Sandia Z machine have been demonstrated to produce high-precision Hugoniot measurements for pressures up to 2 TPa.[28, 29] In addition, the capability to launch layered Al/Cu composite flyers has been shown to enable measurement of the sound velocity along the principal Hugoniot for pressures up to 1.1 TPa.[30-32] Density functional theory (DFT) calculations supplement Hugoniot measurements and provide information on shock temperature and phase to help create a complete EOS for a given material.[29, 30]

Here, we present measurements of the principal Hugoniot of sapphire from 0.18 to 2.1 TPa and sound speed measurements from 0.38 to 1.0 TPa. First-principles molecular dynamics (FPMD) calculations were used to help identify where shock melting occurs and determine whether discrimination between the $CaIrO_3$-type and U_2S_3-type phases was possible. A multi-segment, piecewise linear fit was determined from the Z and gas gun shock velocity – particle velocity Hugoniot data for pressures from 0.1 to 2.1 TPa. Sound speed measurements identified melting between 450 and 530 GPa, and the multi-segment fit to the Hugoniot identified two distinct transitions: from a Rh_2O_3-type phase to $CaIrO_3$-type at ~280 GPa and melting at ~520 GPa. No evidence of a transition from $CaIrO_3$-type to U_2S_3-type was identified, however similarity between the phases precluded discrimination based on sound speed measurements.

Methods

Experimental methods

Plate impact experiments were conducted using the Z machine at Sandia National Laboratories, Albuquerque. Z is a large pulsed-power generator capable of generating currents in excess of 20 MA with rise times ~100-1000 ns.[33, 34] Experiments were conducted using either the coaxial or stripline load geometry with both solid Al or composite Cu/Al flyers. A schematic of a coaxial target using a composite Cu/Al flyer is shown in Figure 1. The nominal thickness of solid Al flyers used was 1.2 mm, and composite flyers were fabricated with 0.9 mm Al and 0.25 mm Cu. Determination of the Cu thickness of an as-fabricated flyer was done by measurement of the mass and final dimensions and calculation of the fraction of Cu and Al from their respective densities. Additional details on flyer fabrication and metrology are given in Refs. 32, 35, 36.

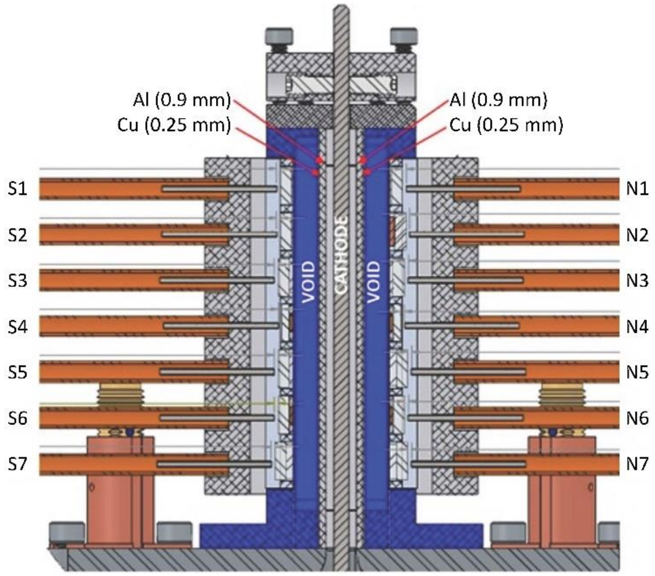

Figure 1: Example schematic of coaxial hardware used for the majority of experiments. The target shown uses the composite Cu/Al flyer which enabled sound speed measurements for some experiments. On other experiments with Al impactors, the thickness is increased to 1.2 mm. As the sapphire samples are transparent, they are typically fielded in the odd-numbered positions, leaving the other locations for additional (typically opaque) materials.

When Z fires, energy stored in the capacitor banks flows through the load and produces a magnetic field within the anode-cathode (A-K) gap. The resultant magnetic field interacts with the current to create a Lorentz force which accelerates the flyer plates across the flight gap and into the samples. The different configurations used in these experiments resulted in impact velocities ranging from 9-41 km/s for Al and 10-27 km/s for Cu/Al[36, 37]. Pulse shapes were optimized to maintain the impact surface of the flyer at ambient conditions.

Samples used in these experiments were HEMEX-grade single-crystal sapphire (Asphera Inc.) cut with the C-axis along the direction of shock propagation. Sample density was measured on a subset of the samples using the Archimedes method and was found to be 3.978±0.011 g/cm^3. Single-crystal Z-cut α-quartz windows were adhered to the back surface of the sapphire samples using an ultra-low-viscosity epoxy (Angstrombond) with average glue thicknesses <1 µm. Polymethylpentene (TPX) windows were used in lieu of quartz for the lowest velocity experiments. Typical sample dimensions were 5×5 mm square with thicknesses ranging from 0.4-1.0 mm. Individual sample thicknesses were measured to <1 µm accuracy.

Flyer velocities and shock velocities were measured with a multipoint velocity interferometer system for any reflector (VISAR) [38, 39] and/or photon Doppler velocimetry (PDV) [40]. The Z VISAR uses a frequency-doubled Nd:YAG laser, operating at 532 nm, and can distribute 38 independent return legs across the various samples tested on each Z experiment. Multiple VISAR etalons were used with vacuum velocities per fringe (VPFs) ranging from 0.26 km/s up to 2.24 km/s. Shock velocity corrections in the sapphire sample and quartz windows used refractive indices of 1.772[41] and 1.547[42], respectively. The uncertainty in the VISAR measurement for a direct velocity measurement was estimated to be 10% of a fringe. Flyer velocities and shock velocities in the quartz windows were directly measured using VISAR. For sample pressures >650 GPa, the shock front in the sapphire was reflective and the shock velocity was also directly measured. Below 650 GPa, the sapphire shock velocity was determined from the shock transit time measured from impact and breakout times. The transit time is determined for all four VISAR quadrature signals independently, resulting in a typical uncertainty of ~0.25 ns. A representative example for the case where the sapphire was not reflective is shown in Figure 2. Measurements of the absolute shock reflectivity were not possible due to variation in the VISAR laser energy and an inability to field a reflectivity standard while observing the flyer velocity.

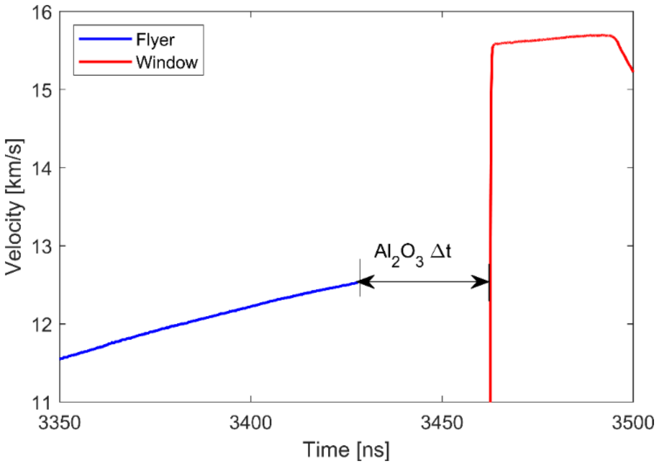

Figure 2: Representative velocimetry data for an experiment where shock front in sapphire is nonreflecting. The flyer velocity (blue) is tracked up to impact upon which the sapphire window becomes opaque. After breakout into a quartz window (red), the shock velocity is directly measured from the reflecting shock front in the quartz. Sapphire shock velocity is determined from the measured transit time (Δt) and thickness.

The sapphire Hugoniot was determined from the shock velocity by using the Monte Carlo impedance matching method[41] with 10^6 iterations and the Rankine-Hugoniot relations[43]. For the aluminum and copper impactors used in these experiments, the $U_S - u_p$ Hugoniot fits and respective covariance matrices used for the standard were taken from Refs. 44 and 32, respectively. Error distributions for the impactor Hugoniot fits were assumed to be Gaussian when calculating the uncertainty for this work.

Sound speed measurements were made using the overtaking rarefaction method.[45] In this method, the overtake time for the rarefaction wave launched from the Cu/Al interface in the flyer is determined in the backing quartz window and related to the sound velocities of the sample, impactor, and window. Details of the method have been described previously.[30-32] The copper $C_S - u_p$ relationship and covariance matrix used to determine the sound speed in the shocked copper were taken from Ref. 32. The arrival time of the rarefaction wave at the drive surface of the sapphire sample is determined from the impact time, shock and sound velocities in the copper and the calculated copper thickness in the flyer. Overtake times in the backing quartz windows were determined by calculating the intersect between fits to the constant velocity plateau and the initial release.

Two or more samples of different thickness were included for shots where sound speeds were measured. This enabled fitting to determine an overtake thickness, d_∞, and overtake time, t_∞, for an arbitrarily thick sample. In this method, the bulk sound speed in both solid and liquid samples and the longitudinal sound speed in solid samples could be determined. The Lagrangian sound speed in this method is given by

$$C_L = \frac{d_\infty}{t_\infty - t_L} \tag{1}$$

where $t_L = t_I - \frac{d_f}{U_S^{Cu}} + \frac{d_f}{C_L^{Cu}}$ is the time when the rarefaction wave enters the sapphire; t_I is the impact time, d_f is the thickness of the copper layer on the flyer, and U_S^{Cu} and C_L^{Cu} are the copper shock velocity and Lagrangian sound velocity, respectively.

A single-sample method was used on two shots in the liquid phase where only one sapphire sample was present. Similar to Refs. 30 and 32 a scale factor between the sapphire sound velocity along the Hugoniot, C_L, and along a partial release curve into the quartz window, C_L^{rel}, was determined from single-sample measurements where the multi-sample technique could also be used. The scale factor was found to be $S_{C_L} = \frac{C_L^{rel}}{C_L} = 0.96 \pm 0.04$. Using this method, the time at which the overtaking rarefaction wave intersects the backwards-propagating rarefaction wave from the quartz window, t_{int}, must first be determined from the overtake time at the sapphire-quartz interface, t_O^I, and the shock breakout time into the quartz window, t_Q: $t_{int} = \frac{S_{C_L} t_O^I + t_Q}{1 + S_{C_L}}$. With this determination, the sound velocity is then calculated using the sample thickness, d_S, as

$$C_L = \frac{d_S}{2t_{int} - (t_Q + t_L)}. \tag{2}$$

Uncertainty in the sound velocity is dominated by the calculated thickness of the copper layer on the composite Cu/Al flyer and the copper Hugoniot and sound velocity. The uncertainty in overtake time in the quartz window was determined by a Monte Carlo method where fitting to the velocity plateau and release used a floating window of 3 ns within user-defined 5 ns regions on either side of the vertex. This resulted in typical overtake time uncertainties <0.25 ns, which is significantly smaller than the typical 40 ns shock transit time for the sapphire samples. Uncertainties in thickness, impact, breakout and overtake times, and copper EOS were propagated with a Monte Carlo method to determine a final uncertainty for the sound velocity measurement. Typical uncertainties calculated using this method were ~6-8%.

FPMD calculations

First-principles molecular dynamics (FPMD) calculations were performed using the Vienna Ab initio Simulation Package (VASP), a plane-wave density functional theory (DFT) code developed at the Technical University of Vienna.[46-48] The aluminum and oxygen atoms in the Hugoniot calculations were represented using the GW projector augmented wave (PAW) potentials[49, 50] and the exchange and correlation were modeled using the revised Perdew-Burke-Ernzerhof (PBE)[51] generalized gradient approximation (PBEsol) functional.[52] The PBEsol functional was chosen for this work because it gave the closest correspondence with the Al_2O_3 ambient state. The plane wave cutoff energy was set to 800 eV. The bulk of the FPMD calculations were carried out with either 60 (corundum, U_2S_3, $CaIrO_3$) or 80 (Rh_2O_3, liquid) atoms in the supercell. Test calculations with 240 atoms in the supercell revealed negligible differences. The molecular dynamics simulations utilized the NVT ensemble with velocity scaling as a prescribed and regulated thermostat and covered on the order of a few to ~20 ps of real time with time steps of 2 fs for the lower pressure and temperature conditions (corundum, Rh_2O_3) and a time step of 1 fs for the higher pressure and temperature conditions (U_2S_3, $CaIrO_3$, liquid). The Brillouin zone was sampled using a 2 x 2 x 2 Monkhorst-Pack **k**-point grid.[53] Hugoniot calculations were performed for the Rh_2O_3, $CaIrO_3$, U_2S_3, and liquid phases.

To determine the principal Hugoniot from the FPMD simulations, the Rankine-Hugoniot relations are used to relate simulated states to the Al_2O_3 ambient state. The Rankine-Hugoniot relations provide a set of equations which can relate the initial energy (E), volume (V), and stress (σ) with steady-state post shock values:

$$(E-E_0)=\frac{1}{2}(\sigma-\sigma_0)(V_0-V) \tag{3}$$

$$(\sigma-\sigma_0)=\rho_0 U_S u_p \tag{4}$$

$$\rho=\frac{\rho_0 U_S}{U_S-u_p} \tag{5}$$

where ρ, U_S and u_p denote the density, shock velocity, and particle velocity, respectively, and the subscript 0 denotes the ambient, unshocked state. Determination of Hugoniot points was done by identifying initial states which are close to satisfying Eq. 3 for the conservation of energy across the shock front then iterating or interpolating in temperature and density to identify a state that satisfies the Rankine-Hugoniot relations. To test convergence of the Hugoniot calculations, additional simulations were conducted to vary the system size, plane wave cutoff, inclusion of spin, a harder potential for the oxygen atoms, and zero-point energy contributions to the reference state. The differences were found to be negligible at the simulated conditions, indicating that the FPMD results are well-converged. The FPMD simulated Hugoniot results are given in Table I.

Table I: FPMD-DFT calculations for the principal Hugoniot of sapphire shock compressed into the Rh_2O_3, $CaIrO_3$, U_2S_3, and liquid phases. V, ρ, P, T, u_p, and U_S are the atomic volume, density, pressure, temperature, particle velocity, and shock velocity, respectively. The simulation of the $CaIrO_3$ phase at 438.3 GPa oscillated between the $CaIrO_3$ and U_2S_3 phases, suggesting that it was near a phase boundary.

Phase	V [Å^3/atom]	ρ [g/cm^3]	P [GPa]	T [K]	u_p [km/s]	U_S [km/s]	Notes
Rh_2O3	6.22	5.44	137.6	1185	3.02	11.23	
Rh_2O3	5.17	6.55	335.3	5700	5.73	14.59	
Rh_2O3	4.88	6.94	438.9	8637	6.84	16.03	
$CaIrO_3$	4.99	6.78	382.8	7500	6.28	15.20	
$CaIrO_3$	4.86	6.97	438.3	8875	6.85	15.97	Phase oscillation with U_2S_3
$CaIrO_3$	4.81	7.04	456.3	9600	7.03	16.20	
$CaIrO_3$	4.70	7.21	510.2	11060	7.56	16.87	Melted
U_2S_3	4.83	7.01	422.7	8500	6.75	15.63	
U_2S_3	4.81	7.04	435.2	8900	6.86	15.78	
U_2S_3	4.76	7.12	459.8	9612	7.11	16.14	
U_2S_3	4.68	7.23	498.4	11000	7.48	16.64	Melted at 11.65 ps
U_2S_3	4.64	7.30	521.2	11450	7.69	16.93	
U_2S_3	4.63	7.31	523.5	11650	7.72	16.95	Melted
U_2S_3	4.57	7.40	560.0	12800	8.05	17.40	Melted
Liquid	4.57	7.40	565.9	10500	8.09	17.49	
Liquid	4.45	7.61	640.5	12375	8.74	18.33	
Liquid	4.20	8.06	834.1	17850	10.28	20.31	
Liquid	4.00	8.46	1029.0	23850	11.69	22.06	
Liquid	3.80	8.91	1277.6	32400	13.31	24.06	

Liquid	3.60	9.40	1602.6	44000	15.23	26.40	

Because a phase oscillation between the $CaIrO_3$ and U_2S_3 phases was observed for the simulation at ~438 GPa, calculations of the Gibbs free energy were carried out for the $CaIrO_3$ and U_2S_3 phases along the 8900K isotherm. Intersection of the free energy curves for the $CaIrO_3$ and U_2S_3 phases indicates that a transition should occur at 435±5 GPa, which agrees well with an extrapolation of the phase boundary predicted by Umemoto and Wentzcovitch.[16] Calculated Hugoniot data indicate that the $CaIrO_3$ phase is less dense than the U_2S_3 phase for a given shock pressure, which may be sufficient to infer the phase when comparing to experimental results. Free energy calculations for the other phase transitions were not conducted in this work.

Sound speeds for the $CaIrO_3$ and U_2S_3 phases were calculated from the elastic constants at pressures close to 400 GPa and temperatures on the principal Hugoniot. To calculate the sound speed, a Hugoniot state was first identified for each phase and the local Grüneisen parameter was calculated to ensure that the strained systems remained on the isentrope. As both phases are orthorhombic, nine independent elastic constants (c11, c12, c13, c22, c23, c33, c44, c55, and c66) were required to be calculated. Small strains (~1% in both compression and tension) were applied to three different strain tensors and the elastic constants were computed by differencing the stresses with the reference Hugoniot state. The three tensors computed produced redundant values for c12, c13, and c23, which enabled confirmation of consistency in the method. Good convergence was obtained with 14000 timesteps for the reference and strained states. Longitudinal and bulk sound speeds and the Poisson ratio were determined from the elastic constants using Voight-Reuss-Hill averages.[54] The calculated sound speeds are given in Table II.

Table II: Bulk (cb) and longitudinal (cl) sound velocities for U2S3 and CaIrO3 phases of alumina at ~400 GPa.

Phase	P [GPa]	T [K]	C_B [km/s]	C_L [km/s]	ν
$CaIrO_3$	397.6	8060	13.93	16.32	0.372
U_2S_3	400.7	7860	13.84	16.22	0.372

The small difference in sound speed between the $CaIrO_3$ and U_2S_3 phases indicates that difficulty in discriminating phases with sound speed data would be expected. In fact, for the nine elastic constants computed to determine a sound speed, seven of them were within a few percent between the two polymorphs; the only two that had noticeable differences were c55 and c66 (softening in c55 and stiffening in c66 in $CaIrO_3$ relative to U2S3). FPMD calculations indicate that x-ray diffraction or high-precision (<2% error) temperature measurements would be required to discriminate between the two phases.

Results

Hugoniot

A total of 68 independent measurements of the pressure and particle velocity in shocked sapphire were used to determine an experimental Hugoniot over the pressure range of 0.18 to 2.1 TPa. The data are shown in Figure 3. Experimentally determined Hugoniot states are given in Table III. This pressure range spans the solid Hugoniot measurements obtained by Erskine[23] and liquid measurements obtained by Hicks *et al*[20] and Ostrik and Nikolaev[6] and form a wide-range EOS for sapphire which is sensitive to phase transitions along the Hugoniot. At pressures below 0.3 TPa, these data agree well with the previous measurements by Erskine[23] obtained using a 2-stage gas gun. There is a discrepancy between these results and the highest-pressure datum from Erskine[23]; this may be related to the use of a Pt rather than Ta impactor for that experiment and potential bowing due to the lower material strength. At pressures above 1.0 TPa, these results agree with those of Hicks *et al*[20] and Ostrik and Nikolaev[6], however the uncertainty in this work is significantly smaller than the previous works. Additionally, scatter in these results is much smaller than that exhibited by the earlier liquid work. The FPMD calculations of the Hugoniot are in excellent agreement with our experimental results over the full pressure range explored.

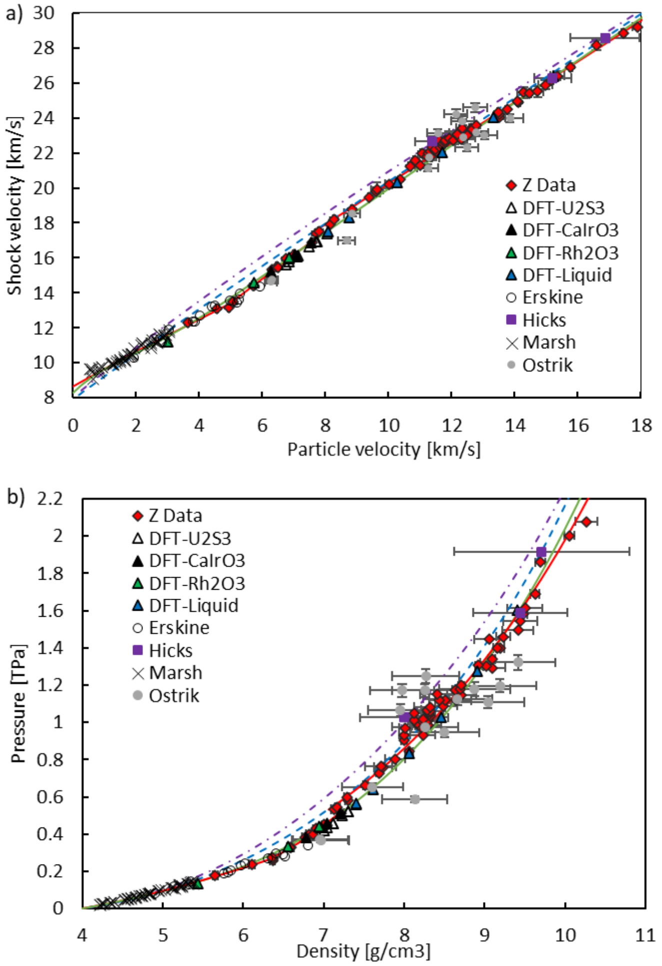

Figure 3: (a) Experimental $U_S - u_p$ Hugoniot results for sapphire from this work (red diamonds), FPMD calculations (triangles) and previous measurements from Refs. 6, 20, 21, 23. Also shown are fits from this work (red), SESAME 7411 (dashed blue), ANEOS 7420 (purple dashed-dotted), and LEOS 2200 (green). A piecewise linear fit was found to best represent the data due to multiple phase transitions. (b) $P - \rho$ plot of the same data as in (a). FPMD calculations from this work and the LEOS table are in excellent agreement for the entire range of the experiments, however the experimental data are slightly stiffer (less compressible) in the liquid just above the melt transition. The ANEOS table does not agree with the experimental results or FPMD calculations.

Table III: Direct-impact Hugoniot from the Z machine for sapphire with Al or Cu/Al impactors. V_f and U_S are the measured flyer plate and shock velocity, respectively. u_p, P, and ρ are the inferred particle velocity, pressure, and density, respectively. Experiments with measured velocities given to 0.1 m/s precision used an older (and less precise) measurement system.

Flyer material	V_f **[km/s]**	U_S **[km/s]**	u_p **[km/s]**	P **[GPa]**	ρ **[g/cm^3]**
Al	8.90 ± 0.03	12.31 ± 0.12	3.64 ± 0.03	178.6 ± 1.5	5.65 ± 0.04
Al	10.92 ± 0.03	13.11 ± 0.07	4.56 ± 0.03	238.1 ± 1.9	6.11 ± 0.06
Al	11.61 ± 0.03	13.14 ± 0.06	4.93 ± 0.03	257.8 ± 1.9	6.37 ± 0.06
Al	11.98 ± 0.04	13.48 ± 0.14	5.06 ± 0.04	271.6 ± 2.5	6.38 ± 0.08
Al	12.00 ± 0.05	13.53 ± 0.12	5.07 ± 0.05	272.9 ± 2.6	6.36 ± 0.07
Al	13.51 ± 0.01	14.42 ± 0.06	5.72 ± 0.03	328.1 ± 2.1	6.60 ± 0.05
Al	13.50 ± 0.05	14.45 ± 0.09	5.71 ± 0.04	328.4 ± 2.7	6.58 ± 0.07
Cu/Al	10.51 ± 0.04	15.31 ± 0.03	6.30 ± 0.03	384.0 ± 1.8	6.76 ± 0.02
Cu/Al	10.76 ± 0.04	15.51 ± 0.04	6.45 ± 0.03	398.5 ± 1.9	6.82 ± 0.03
Cu/Al	10.80 ± 0.04	15.43 ± 0.07	6.49 ± 0.03	398.7 ± 2.2	6.87 ± 0.04
Cu/Al	11.26 ± 0.04	15.95 ± 0.07	6.75 ± 0.03	428.7 ± 2.3	6.90 ± 0.04
Al	16.46 ± 0.03	16.10 ± 0.04	7.01 ± 0.04	448.9 ± 2.8	7.05 ± 0.05
Cu/Al	11.65 ± 0.04	16.19 ± 0.06	7.00 ± 0.03	450.9 ± 2.2	7.01 ± 0.03
Al	17.81 ± 0.02	16.91 ± 0.05	7.59 ± 0.04	510.5 ± 3.2	7.22 ± 0.05
Cu/Al	12.86 ± 0.04	17.42 ± 0.12	7.69 ± 0.03	533.3 ± 3.3	7.13 ± 0.06
Cu/Al	13.04 ± 0.04	17.54 ± 0.11	7.81 ± 0.03	544.8 ± 3.1	7.17 ± 0.05
Cu/Al	13.60 ± 0.04	17.93 ± 0.04	8.15 ± 0.03	581.6 ± 2.3	7.30 ± 0.03
Cu/Al	13.82 ± 0.04	18.22 ± 0.09	8.27 ± 0.03	600.0 ± 2.9	7.29 ± 0.04
Cu/Al	14.73 ± 0.04	18.79 ± 0.02	8.85 ± 0.03	661.8 ± 2.3	7.52 ± 0.02
Cu/Al	15.62 ± 0.04	19.48 ± 0.02	9.39 ± 0.03	728.0 ± 2.4	7.69 ± 0.02
Al	22.55 ± 0.19	19.80 ± 0.14	9.62 ± 0.11	757.8 ± 8.8	7.74 ± 0.11
Al	22.6 ± 0.3	19.9 ± 0.4	9.62 ± 0.19	762.2 ± 15.8	7.71 ± 0.25
Al	23.4 ± 0.2	20.2 ± 0.2	10.01 ± 0.12	804.5 ± 10.1	7.89 ± 0.14
Al	24.12 ± 0.02	20.46 ± 0.06	10.36 ± 0.05	843.4 ± 5.1	8.06 ± 0.06
Cu/Al	17.75 ± 0.05	21.24 ± 0.02	10.67 ± 0.04	902.1 ± 3.2	8.00 ± 0.03
Al	25.6 ± 0.3	21.3 ± 0.2	11.01 ± 0.16	933.0 ± 13.6	8.23 ± 0.17
Cu/Al	18.08 ± 0.09	21.60 ± 0.11	10.86 ± 0.07	933.5 ± 6.6	8.00 ± 0.0
Cu/Al	18.45 ± 0.09	22.00 ± 0.11	11.07 ± 0.07	969.1 ± 6.8	8.01 ± 0.07
Al	26.2 ± 0.2	21.8 ± 0.2	11.23 ± 0.1	974.6 ± 11.2	8.21 ± 0.15
Cu/Al	18.70 ± 0.09	21.95 ± 0.11	11.26 ± 0.07	983.3 ± 6.9	8.17 ± 0.08
Al	26.4 ± 0.3	21.8 ± 0.2	11.35 ± 0.16	984.5 ± 14.1	8.30 ± 0.18
Cu/Al	18.80 ± 0.05	22.08 ± 0.02	11.31 ± 0.04	993.8 ± 3.4	8.16 ± 0.03
Al	26.7 ± 0.3	22.2 ± 0.2	11.44 ± 0.15	1008.4 ± 13.8	8.23 ± 0.17
Cu/Al	18.94 ± 0.09	22.30 ± 0.11	11.38 ± 0.07	1009.9 ± 7.1	8.13 ± 0.07
Al	26.8 ± 0.3	22.1 ± 0.2	11.51 ± 0.16	1012.0 ± 14.7	8.30 ± 0.18
Al	26.8 ± 0.3	22.2 ± 0.2	11.48 ± 0.18	1015.2 ± 16.0	8.23 ± 0.17
Al	27.1 ± 0.3	22.3 ± 0.2	11.63 ± 0.16	1032.3 ± 14.9	8.32 ± 0.18
Cu/Al	19.39 ± 0.10	22.42 ± 0.11	11.69 ± 0.07	1042.8 ± 7.4	8.31 ± 0.08
Al	27.2 ± 0.3	22.7 ± 0.4	11.59 ± 0.19	1048.5 ± 18.6	8.12 ± 0.25
Cu/Al	19.50 ± 0.10	22.56 ± 0.11	11.75 ± 0.07	1054.6 ± 7.4	8.30 ± 0.08
Al	27.5 ± 0.3	22.6 ± 0.2	11.79 ± 0.16	1060.5 ± 15.1	8.32 ± 0.17

Cu/Al	19.60 ± 0.10	22.70 ± 0.11	11.80 ± 0.07	1065.9 ± 7.5	8.29 ± 0.08
Al	27.8 ± 0.3	22.8 ± 0.4	11.91 ± 0.19	1082.0 ± 18.9	8.32 ± 0.27
Al	28.0 ± 0.3	22.7 ± 0.2	12.05 ± 0.17	1088.8 ± 15.9	8.48 ± 0.19
Al	28.4 ± 0.2	23.0 ± 0.2	12.22 ± 0.13	1116.4 ± 12.0	8.51 ± 0.15
Al	28.5 ± 0.3	22.8 ± 0.2	12.31 ± 0.18	1117.4 ± 16.5	8.65 ± 0.20
Al	28.4 ± 0.2	23.1 ± 0.2	12.19 ± 0.12	1120.3 ± 12.0	8.43 ± 0.15
Al	28.9 ± 0.3	23.0 ± 0.2	12.50 ± 0.18	1143.9 ± 16.7	8.71 ± 0.20
Al	28.8 ± 0.3	23.4 ± 0.5	12.34 ± 0.21	1150.9 ± 21.3	8.41 ± 0.32
Al	29.25 ± 0.05	23.39 ± 0.04	12.61 ± 0.04	1173.5 ± 3.8	8.63 ± 0.04
Al	29.33 ± 0.04	23.35 ± 0.03	12.66 ± 0.04	1176.6 ± 3.4	8.69 ± 0.03
Al	29.63 ± 0.05	23.55 ± 0.04	12.79 ± 0.04	1198.4 ± 3.9	8.71 ± 0.04
Al	31.11 ± 0.28	24.04 ± 0.11	13.52 ± 0.17	1293.3 ± 16.1	9.09 ± 0.16
Al	31.17 ± 0.05	24.19 ± 0.03	13.52 ± 0.04	1301.5 ± 4.2	9.02 ± 0.04
Al	31.16 ± 0.05	24.33 ± 0.04	13.48 ± 0.04	1305.3 ± 4.3	8.92 ± 0.04
Al	31.70 ± 0.05	24.47 ± 0.03	13.76 ± 0.04	1339.8 ± 4.3	9.09 ± 0.04
Al	32.50 ± 0.05	24.89 ± 0.04	14.12 ± 0.05	1398.5 ± 4.6	9.20 ± 0.05
Al	32.48 ± 0.05	24.94 ± 0.04	14.09 ± 0.05	1399.0 ± 4.6	9.15 ± 0.05
Al	33.0 ± 0.3	25.5 ± 0.3	14.27 ± 0.19	1445.7 ± 20.4	9.06 ± 0.24
Cu/Al	23.80 ± 0.12	25.40 ± 0.13	14.45 ± 0.09	1460.5 ± 10.4	9.23 ± 0.11
Al	33.8 ± 0.3	25.5 ± 0.3	14.72 ± 0.19	1494.2 ± 207	9.42 ± 0.27
Al	34.40 ± 0.34	25.89 ± 0.26	14.98 ± 0.21	1543.1 ± 22.8	9.44 ± 0.26
Al	34.86 ± 0.05	26.16 ± 0.04	15.17 ± 0.05	1580.0 ± 5.3	9.48 ± 0.05
Al	35.25 ± 0.35	26.40 ± 0.26	15.34 ± 0.22	1612.1 ± 23.9	9.50 ± 0.26
Al	36.20 ± 0.05	26.89 ± 0.04	15.77 ± 0.05	1688.1 ± 5.8	9.63 ± 0.05
Cu/Al	27.32 ± 0.05	28.16 ± 0.26	16.59 ± 0.06	1859.7 ± 13.7	9.69 ± 0.17
Al	39.90 ± 0.05	28.87 ± 0.04	17.44 ± 0.06	2003.4 ± 7.1	10.05 ± 0.06
Al	40.80 ± 0.20	29.20 ± 0.15	17.88 ± 0.14	2077.8 ± 16.5	10.27 ± 0.17

In the shock velocity – particle ($U_S - u_p$) velocity frame, multiple distinct regions can be identified where the Hugoniot appears to change slope. This behavior is expected as sapphire has been predicted to undergo multiple phase changes along the Hugoniot. A piecewise linear fit was determined using the $U_S - u_p$ data and optimized to determine locations of kinks in the data, indicative of phase boundaries. Umemoto and Wentzcovitch[16] predicted that the shock Hugoniot would cross three phase boundaries prior to melting: corundum → Rh_2O_3, Rh_2O_3 → $CaIrO_3$, and $CaIrO_3$→ U_2S_3. Comparison between our experimental data and the FPMD simulations indicated that we would be unable to distinguish between the $CaIrO_3$ and U_2S_3 phases due to a small density difference of 1%. For this reason, we chose to fit the Hugoniot using three solid regions, corundum, Rh_2O_3, and $CaIrO_3/U_2S_3$, and one liquid phase. The data used to determine the Hugoniot consisted of that of Marsh,[21] Erskine,[23] and this work. For the weighted linear fits, uncertainties of 3% and 1% were assumed for the Marsh and the Erskine data, respectively, based on the diagnostics available at the time of those experiments. Identification of the transition points was done by minimizing the uncertainty-weighted regression sum of squares while using a sliding window across the experimental results for the location of the transition points in the fit.

For the transition point from corundum → Rh_2O_3, we used the pressure of 79±2 GPa identified by Mashimo *et al*[14] from inclined mirror experiments; this corresponds to a particle velocity of $u_p = 1.881 \pm 0.041\ km/s$. Identified transition points for the Rh_2O_3 → $CaIrO_3/U_2S_3$ and $CaIrO_3/U_2S_3$ → liquid transitions were determined to be $u_p = 5.065 \pm 0.050\ km/s$ and $u_p = 7.639 \pm 0.054\ km/s$, respectively. These particle velocities correspond to phase transition pressures of 272±5 GPa and 525±13 GPa, respectively. The transition pressure from Rh_2O_3 → $CaIrO_3$ agrees well with a comparison of FPMD pressure-compression curves and the Erskine data.[16] Best-fit parameters for the least-squares linear fits and covariance matrices for the four regions are given in Table IV.

Table IV: Fit and covariance matrix parameters for 4-segment piecewise linear Hugoniot of sapphire in form $U_S = C_0 + Su_p$.

Phase	C_0 [km/s]	S	$\sigma_{C_0}^2$ ($\times 10^{-3}$)	σ_S^2 ($\times 10^{-4}$)	$\sigma_{C_0}\sigma_S$ ($\times 10^{-3}$)
Corundum	8.667	1.003	18.03	106.7	-12.75
Rh_2O_3	8.817	0.920	11.46	7.976	-2.917
$CaIrO_3$	6.585	1.372	43.32	10.41	-6.684
Liquid	8.621	1.163	4.123	0.2887	-0.3382

Results were compared against Hugoniots calculated from the SESAME (7411),[55] ANEOS (7420),[56] and LEOS (2200)[57, 58] databases. For pressures below those of achieved in the present work, all three tables reasonably reproduce the experimental data. At the time of construction for the SESAME 7411 and ANEOS 7420 tables, the data from Marsh was the only existing measurements to constrain the high-pressure behavior. The SESAME 7411 table is in reasonable agreement with these data for pressures >500 GPa, corresponding to the liquid phase. The SESAME 7411 Hugoniot appears to stiffen at high pressure, which indicates that it has an incorrect derivative of bulk modulus with respect to density. Regardless, the SESAME 7411 table significantly outperforms the ANEOS 7420 table, which is significantly stiffer than the data over the entire range of pressures studied in this work (Fig. 3b).

The LEOS 2200 Hugoniot agrees well with data over the solid range (<500 GPa) and the liquid range above 1000 GPa. At intermediate pressures (500-1000 GPa), the LEOS Hugoniot is slightly stiffer (2-3% in density) than the experimental results. This discrepancy is likely due to the LEOS table being a single-phase rather than multi-phase table and smoothly interpolating between the low-pressure and high-pressure behavior. Because none of the tabular EOS models accurately represent the experimental and FPMD results over the entire pressure range, a new multi-phase EOS table is warranted for hydrocode modeling of experiments using sapphire as a sample or window material.

Sound Velocity

A subset of Z experiments used composite Cu/Al flyers, which enabled wave speeds to be determined in the sapphire samples. We note that some of the Cu/Al flyer experiments either lost contrast or suffered from anomalous late-time noise in the VISAR record, which precluded the determination of wave speeds. Sound velocity measurements are given in Table V, and the bulk (red diamonds) and longitudinal (yellow diamonds) sound velocities are shown in Figure 4. The Grüneisen parameter (Γ) was calculated from the bulk sound velocities and the Hugoniot fits for the specific phase.

Table V: Measured bulk (C_B) and longitudinal (C_L) sound speeds for shock-compressed sapphire. The Grüneisen parameter (Γ) was calculated from the bulk sound speed and Hugoniot fit.

State	P [GPa]	ρ [g/cm³]	C_B [km/s]	C_L [km/s]	Γ
Solid	384.0 ± 1.8	6.76 ± 0.02	14.98 ± 0.80	16.52 ± 0.45	0.83 ± 0.35

Solid	398.5 ± 1.9	6.82 ± 0.03	14.51 ± 0.37	17.01 ± 0.51	1.09 ± 0.17
Solid	398.7 ± 2.2	6.87 ± 0.04	14.98 ± 0.43	16.35 ± 0.62	0.97 ± 0.20
Solid	428.7 ± 2.3	6.90 ± 0.04	15.39 ± 0.37	16.99 ± 0.51	0.86 ± 0.18
Solid	450.9 ± 2.2	7.01 ± 0.03	15.85 ± 0.47	16.59 ± 0.45	0.83 ± 0.21
Liquid	533.3 ± 3.3	7.13 ± 0.06	16.53 ± 0.62	**	0.38 ± 0.26
Liquid	544.8 ± 3.1	7.17 ± 0.05	16.56 ± 0.51	**	0.42 ± 0.20
Liquid	600.0 ± 2.9	7.29 ± 0.04	17.03 ± 0.77	**	0.34 ± 0.29
Liquid	661.8 ± 2.3	7.52 ± 0.02	17.60 ± 0.68	**	0.34 ± 0.22
Liquid	728.0 ± 2.4	7.69 ± 0.02	18.31 ± 0.70	**	0.25 ± 0.21

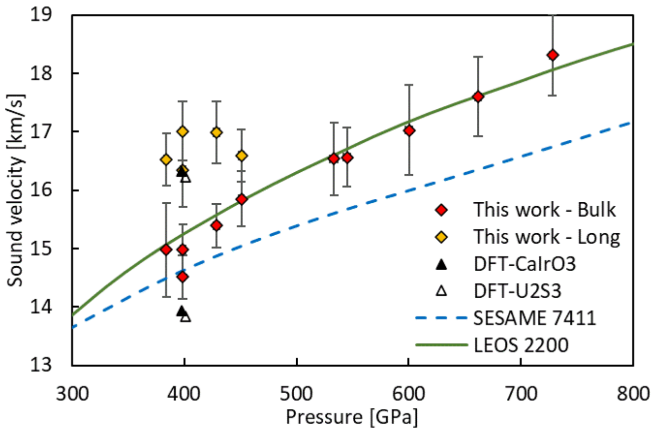

Figure 4: Sapphire sound velocity as function of shock pressure. The bulk (red diamonds) sound velocity is in good agreement with the LEOS 2200 (green) model, whereas the SESAME 7411 (dashed blue) model underpredicts the sound velocity. Longitudinal (yellow diamonds) velocities were measured for experiments below 450 GPa, confirming that melt occurs near 500 GPa. FPMD sound velocities for CaIrO$_3$ (solid triangles) and U$_2$S$_3$ (open triangles) lie on top of one another and are within the uncertainty of the measured longitudinal wave speed, but systematically lower than the bulk velocities.

As was predicted from the FPMD results, the difference in sound velocity between the CaIrO$_3$ and U$_2$S$_3$ phases at ~400 GPa appears to be too small to discriminate between the phases. The FPMD calculations for both the CaIrO$_3$ phase (filled triangles) and U$_2$S$_3$ phase (open triangles) overlap with one another for both the bulk and longitudinal velocities. This highlights the need for phase-sensitive measurements, such as x-ray diffraction, to probe solid-solid phase transitions within a crystal. However, the experimental results identify the absence of a longitudinal wave for the experiments above 530 GPa, which agrees with the pressure at which melting was identified from the $U_S - u_p$ Hugoniot data and provides additional evidence for the location of the melt transition.

The experimental results were compared to the FPMD calculations and SESAME 7411 and LEOS 2200 models. The ANEOS 7420 model was excluded from this comparison due to its significantly stiffer Hugoniot behavior (Figure 3). Experimental longitudinal wave speeds exceed the bulk wave speeds in compressed sapphire by 10-16%, which agrees with the difference predicted by the FPMD calculations. However, the experimental results are ~8% greater than the FPMD calculations for both the bulk and longitudinal wave speeds. This is consistent with previous work on beryllium[31] and bridgmanite[30] where it was found that FPMD systematically underpredicted the sound velocity measured in these overtaking wave experiments. At the pressures of these experiments, the sound velocity of the copper standard is well-constrained with experimental data, so it is not a likely source of the discrepancy. Two main sources for the discrepancy exist in the FPMD calculations: assumption of an isotropic Hugoniot state to determine a sound velocity from the elastic constants, and the functionals used in the calculations. The first source is likely the dominant source of the discrepancy because the Voigt-Reuss-Hill average assumes that at the Hugoniot state, the material is isotropic and polycrystalline, whereas our samples were single crystals. Previous work by Kanel *et al*[59] demonstrated that the Hugoniot elastic limit of shocked sapphire and ambient sound velocity is greater along the C-axis than other orientations, so these calculations would underpredict the sound velocity along the C-axis by ~2%, which puts the calculated values within the experimental uncertainty.

The SESAME 7411 model predicts a similar trend in the $C_S - P$ plane to the data reported here but is systematically low in the liquid regime. In the solid regime, the uncertainty in the measurements overlaps with the SESAME model prediction. This suggests that the SESAME 7411 model accurately predicts the derivative of the bulk modulus with respect to pressure but has an incorrect reference state for the liquid compressibility. The LEOS 2200 model is in excellent agreement with the experimental data for the entirety of the region where data exists. To investigate the discrepancy between the SESAME 7411 model prediction and the data further, the bulk sound speed was plotted as a function of density (Figure 5). In the $C_S - P$ plane, there is a noticeable difference in slope between the SESAME and LEOS models, and the experimental data trends with the LEOS model. This confirms the inference made from the Hugoniot data regarding the derivative of the bulk modulus with respect to density; the SESAME 7411 model underpredicts $\frac{d\mathrm{K}}{d\rho}$, so an update to the model is necessary.

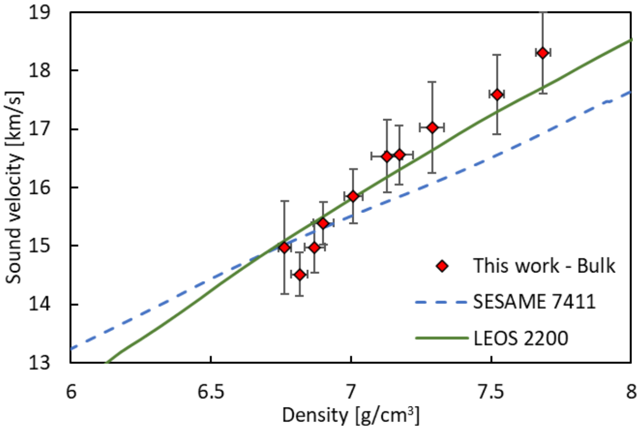

Figure 5: Comparing the sound velocity to the shock density indicates that the SESAME 7411 model (dashed blue) slope is shallower than the experimental measurements (red diamonds) and LEOS 2200 model. This suggests that the derivative of the bulk modulus with respect to density is underpredicted by the SESAME model.

Discussion

The $U_S - u_p$ relations given in Table IV provide a starting point to constrain the sapphire phase diagram at high pressure, as shown in Figure 6. In conjunction with temperature calculations from FPMD and temperature data at the melt curve by Ostrik and Nikolaev, we can constrain the high-pressure phase diagram along the principal Hugoniot up to the completion of melt. We note that the melt curve calculated by Ostrik and Nikolaev only used the corundum phase, so measurements or calculations for the high-pressure phases are needed. Previous FPMD calculations using the local density approximation (LDA) and generalized gradient approximation (GGA) have differed by ~30 GPa on the pressure at which the transformation occurs at various temperatures.[17] Static high-pressure experiments in laser-heated diamond anvil cell (DACs)[10-12] have identified the transitions from the corundum → Rh_2O_3 and Rh_2O_3 → $CaIrO_3$ phases, however the transition pressure for the latter differs significantly between published results and is hypothesized as being related to thermal nonuniformities due to gold powder in the cell.[11, 12] In addition, the corundum → Rh_2O_3 phase transition has been previously identified in shock experiments,[14] but does not agree with DAC measurements.

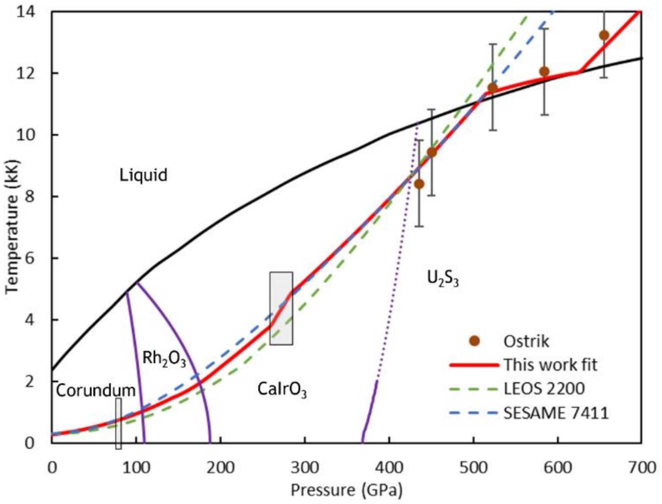

Figure 6: High temperature-pressure phase diagram of sapphire. The boundaries between solid phases (purple) are from GGA calculations and shifted to match experimental data. The dotted boundary between $CaIrO_3$ and U_2S_3 extrapolates the GGA calculation to intersect the DFT calculation from this work. The melt curve (black) is from Ostrik and Nikolaev. Gray boxes represent locations where phase transitions were identified in shock experiments

Phase boundaries between the solid phases (purple lines in Figure 6) are based on the GGA calculations by Tsuchiya[17] as those are in better agreement with the experimental work by Kato *et al*[12] than their LDA calculations. The transition between the Rh_2O_3 and $CaIrO_3$ phases was adjusted to higher pressure for the GGA calculation to match the measured transition. As Kato *et al* maintained a steady state and allowed for the transition to occur, we believe that their results are the most representative of the equilibrium phase boundary. Shock-identified phase transitions are indicated by the gray boxes on the phase diagram. The proposed $CaIrO_3$ → U_2S_3 transition was extrapolated to pass through the transition determined by the intersection of the Gibbs free energy along the 8900K isotherm for the two phases in this work. The Hugoniot temperatures for this work (red line) are determined by fitting the temperatures from the FPMD calculations after excluding simulations where phase oscillations or melting occurred. The transition locations are determined from the $U_S - u_p$ fits. The broad transition regions for Rh_2O_3 → $CaIrO_3$ and the completion of melt were approximated using the width of the transition region from Kato[12] and temperature data from Ostrik and Nikolaev,[6] respectively. Temperatures along the Hugoniot in the transition regions are interpolated between the temperatures from the respective phases. This likely does not accurately represent the temperature in a mixed phase regime and full kinetic simulations of the transition are warranted. The temperatures calculated by FPMD are in excellent agreement with the experimental results from Ostrik and Nikolaev.

The large discrepancy between the identified transition pressure for the Rh_2O_3 → $CaIrO_3$ transition implies that kinetic effects likely play a significant role. This supposition is supported by the DAC experiments by Kato where they identified that the transition was sluggish and required maintaining approximately constant $P - T$ conditions for ~30 minutes. Due to the potential for significant kinetic hindering, the DAC results from Kato should be assumed to be representative of the equilibrium phase boundary and the shock transition does not imply that a revision of the equilibrium phase boundary is necessary. Assuming kinetic hindering of the transition implies that significant overpressure is necessary to observe the phase transition during the ~ns timescale of a shock experiment; this agrees with the experimental results. Kinetic modeling to understand the $Rh_2O_3 \rightarrow CaIrO_3$ phase transition mechanism could provide interesting insight as to behavior of alumina at high pressure.

Conclusion

The principal Hugoniot and sound velocity of shock-compressed sapphire was measured using magnetically-launched flyer plates on the Z machine. Copper and aluminum impactors were used to shock the sapphire to pressures ranging from 0.2 to 2.1 TPa. Hugoniot measurements are in good agreement with previous experimental data and provide significant improvement in precision. The experimental results agree well with the LEOS 2200 model outside of 500-800 GPa, which corresponds to a mixed solid-liquid phase and liquid alumina near the melt temperature. The SESAME 7411 model agrees well with experimental measurements in the liquid but is too stiff to accurately model the solid. A four-segment piecewise linear fit was found to best reproduce the Hugoniot results. This fit comprises separate regions for the corundum, Rh_2O_3, $CaIrO_3$, and liquid phases. No experimental evidence was found to justify a separate fit for the proposed U_2S_3 phase. Shock melting was identified from a kink in the $U_S - u_p$ Hugoniot at 525 ± 13 GPa.

The sound velocity was determined using the overtaking rarefaction method for samples impacted with composite Cu/Al flyers. Sound velocities were measured over the range 380-730 GPa to investigate the proposed $CaIrO_3 \rightarrow U_2S_3$ phase transition and shock melting. A clear signature for a two-wave release structure from solid material is present below 460 GPa and a single release from liquid material is observed above 530 GPa. This agrees with the melt determination from the kink in the $U_S - u_p$ Hugoniot observed at 525 GPa. FPMD calculations of the sound speed in $CaIrO_3$ and U_2S_3 suggest that the sound speed experiments would be unable to discriminate between those two phases. This agrees with expected difference in sound velocity from Birch's law due to the small density difference.

An updated phase diagram, which incorporates the various solid phases and shock melting, was presented. The solid-solid transitions were modified from GGA calculations to match experimental data from diamond anvil cell experiments. The Hugoniot was fit to FPMD calculations and the solid-liquid mixed phase region was identified from the onset of melt and previous shock temperature data. The shock-driven $Rh_2O_3 \rightarrow CaIrO_3$ phase transition occurs at significantly higher pressure than that observed in static experiments. The observed transition is not believed to be representative of an equilibrium phase transition and the difference between the static and dynamic work is conjectured to be due to kinetic hindering.

Acknowledgements

We thank Heath Hanshaw, Ray Lemke, and Jeremy Boerner for pulseshaping support, Jeff Gluth, Ed Scoglietti, Tom Avila, and Chris De La Cruz for VISAR and PDV support, and Kyle Cochrane and Josh Townsend for useful discussions.

This article has been authored by an employee of National Technology & Engineering Solutions of Sandia, LLC under Contract No. DE-NA0003525 with the U.S. Department of Energy (DOE). The employee owns all right, title and interest in and to the article and is solely responsible for its contents. The United

References

1. B. J. Jensen, D. B. Holtkamp, P. A. Rigg and D. H. Dolan, J. Appl. Phys. **101** (1), 013523 (2007).
2. S. C. Jones, M. C. Robinson and Y. M. Gupta, J. Appl. Phys. **93** (2), 1023-1031 (2003).
3. H. K. Mao, P. M. Bell, J. W. Shaner and D. J. Steinberg, J. Appl. Phys. **49** (6), 3276-3283 (1978).
4. S. T. Weir, A. C. Mitchell and W. J. Nellis, Phys. Rev. Lett. **76** (11), 1860–1863 (1996).
5. C. T. Seagle, W. D. Reinhart, A. J. Lopez, R. J. Hickman and T. F. T. III, J. Appl. Phys. **120** (12), 125902 (2016).
6. A. Ostrik and D. Nikolaev, J. Phys.: Conf. Ser. **2154** (1), 012010 (2022).
7. T. Irifune, Nature **370** (6485), 131-133 (1994).
8. J. Li, V. V. Struzhkin, H.-k. Mao, J. Shu, R. J. Hemley, Y. Fei, B. Mysen, P. Dera, V. Prakapenka and G. Shen, Proc. Nat. Acad. Sci. **101** (39), 14027-14030 (2004).
9. T. Irifune, T. Koizumi and J.-i. Ando, Physics of the Earth and Planetary Interiors **96** (2), 147-157 (1996).
10. J.-F. Lin, O. Degtyareva, C. T. Prewitt, P. Dera, N. Sata, E. Gregoryanz, H.-k. Mao and R. J. Hemley, Nature Materials **3** (6), 389-393 (2004).
11. S. Ono, A. R. Oganov, T. Koyama and H. Shimizu, Earth and Planetary Science Letters **246** (3), 326-335 (2006).
12. J. Kato, K. Hirose, H. Ozawa and Y. Ohishi, American Mineralogist **98** (2-3), 335-339 (2013).
13. N. Funamori and R. Jeanloz, Science **278** (5340), 1109-1111 (1997).
14. T. Mashimo, K. Tsumoto, K. Nakamura, Y. Noguchi, K. Fukuoka and Y. Syono, Geophys. Res. Lett. **27** (14), 2021-2024 (2000).
15. A. Hari, R. Hari, P. G. Heighway, R. F. Smith, T. S. Duffy, M. Sims, S. Singh, D. E. Fratanduono, C. A. Bolme, A. E. Gleason, F. Coppari, H. J. Lee, E. Granados, P. Heimann, J. H. Eggert and J. K. Wicks, J. Phys.: Condensed Matter **35** (9), 094002 (2023).
16. K. Umemoto and R. M. Wentzcovitch, Proc. Nat. Acad. Sci. **105** (18), 6526-6530 (2008).
17. J. Tsuchiya, T. Tsuchiya and R. M. Wentzcovitch, Phys. Rev. B **72** (2), 020103 (2005).
18. G. Shen and P. Lazor, J. Geophys. Res.: Solid Earth **100** (B9), 17699-17713 (1995).
19. Z. Wang, H. Mao and S. K. Saxena, Journal of Alloys and Compounds **299** (1), 287-291 (2000).
20. D. G. Hicks, P. M. Celliers, G. W. Collins, J. H. Eggert and S. J. Moon, Phys. Rev. Lett. **91** (3), 035502 (2003).
21. S. P. Marsh, *LASL Shock Hugoniot Data*. (University of California Press, Berkeley, CA, 1980).
22. R. A. Graham and W. P. Brooks, J. Phys. Chem. Solids **32** (10), 2311-2330 (1971).
23. D. Erskine, AIP Conf. Proc. **309** (1), 141-143 (1994).
24. W. D. Reinhart, L. C. Chhabildas and T. J. Vogler, Int. J. Impact. Engin. **33** (1), 655-669 (2006).
25. G. J. Kleiser, L. C. Chhabildas and W. D. Reinhart, Int. J. Impact. Engin. **38** (6), 473-479 (2011).
26. L. M. Barker and R. E. Hollenbach, J. Appl. Phys. **41** (10), 4208-+ (1970).
27. W. J. Nellis, G. I. Kanel, S. V. Razorenov, A. S. Savinykh and A. M. Rajendran, J. Phys.: Conf. Ser. **215**, 012148 (2010).

28. M. D. Knudson and M. P. Desjarlais, Phys. Rev. Lett. **103** (22), 225501 (2009).

29. K. R. Cochrane, P. Kalita, J. L. Brown, C. A. McCoy, J. W. Gluth, H. L. Hanshaw, E. Scoglietti, M. D. Knudson, S. P. Rudin and S. D. Crockett, Phys. Rev. B **105** (22), 224109 (2022).

30. Y. Fei, C. T. Seagle, J. P. Townsend, C. A. McCoy, A. Boujibar, P. Driscoll, L. Shulenburger and M. D. Furnish, Nature Communications **12** (1), 876 (2021).

31. C. A. McCoy, M. D. Knudson and M. P. Desjarlais, Phys. Rev. B **100**, 054107 (2019).

32. C. A. McCoy, M. D. Knudson and S. Root, Phys. Rev. B **96**, 174109 (2017).

33. M. E. Savage, L. F. Bennett, D. E. Bliss, W. T. Clark, R. S. Coats, J. M. Elizondo, K. R. LeChien, H. C. Harjes, J. M. Lehr, J. E. Maenchen, D. H. McDaniel, M. F. Pasik, T. D. Pointon, A. C. Owen, D. B. Seidel, D. L. Smith, B. S. Stoltzfus, K. W. Struve, W. A. Stygar, L. K. Warne, J. R. Woodworth, C. W. Mendel, K. R. Prestwich, R. W. Shoup, D. L. Johnson, J. P. Corley, K. C. Hodge, T. C. Wagoner and P. E. Wakeland, 2007 16th IEEE International Pulsed Power Conference **2**, 979-984 (2007).

34. D. B. Sinars, M. A. Sweeney, C. S. Alexander, D. J. Ampleford, T. Ao, et al, Phys. Plasmas **27** (7), 070501 (2020).

35. M. D. Knudson, R. W. Lemke, D. B. Hayes, C. A. Hall, C. Deeney and J. R. Asay, J. Appl. Phys. **94** (7), 4420-4431 (2003).

36. R. W. Lemke, M. D. Knudson and J.-P. Davis, Int. J. Impact. Engin. **38** (6), 480-485 (2011).

37. R. W. Lemke, M. D. Knudson, D. E. Bliss, K. Cochrane, J.-P. Davis, A. A. Giunta, H. C. Harjes and S. A. Slutz, J. Appl. Phys. **98** (7), 073530 (2005).

38. L. M. Barker and R. E. Hollenbach, J. Appl. Phys. **43** (11), 4669–4675 (1972).

39. L. M. Barker and K. W. Schuler, J. Appl. Phys. **45** (8), 3692–3693 (1974).

40. D. H. Dolan and S. C. Jones, Rev. Sci. Instrum. **78** (7), 076102 (2007).

41. I. H. Malitson, Journal of the Optical Society of America **52** (12), 1377-1379 (1962).

42. G. Ghosh, Optics Communications **163** (1), 95-102 (1999).

43. Y. B. Zel'dovich and Y. P. Raizer, *Physics of Shock Waves and High-Temperature Hydrodynamic Phenomena*. (Dover Publications, 2002).

44. S. Root, T. R. Mattsson, K. Cochrane, R. W. Lemke and M. D. Knudson, J. Appl. Phys. **118** (20), 205901 (2015).

45. L. V. Al'Tshuler, S. B. Kormer, M. I. Brazhnik, L. A. Vladimirov, M. P. Speranskaya and A. I. Funtikov, Sov. Phys. JETP **11** (4), 766 (1960).

46. G. Kresse and J. Hafner, Phys. Rev. B **47**, 558-561 (1993).

47. G. Kresse and J. Hafner, Phys. Rev. B **49** (20), 14251-14269 (1994).

48. G. Kresse and J. Furthmüller, Phys. Rev. B **54** (16), 11169-11186 (1996).

49. P. E. Blöchl, Phys. Rev. B **50** (24), 17953-17979 (1994).

50. G. Kresse and D. Joubert, Phys. Rev. B **59** (3), 1758-1775 (1999).

51. J. P. Perdew, K. Burke and M. Ernzerhof, Phys. Rev. Lett. **77** (18), 3865-3868 (1996).

52. J. P. Perdew, A. Ruzsinszky, G. I. Csonka, O. A. Vydrov, G. E. Scuseria, L. A. Constantin, X. Zhou and K. Burke, Phys. Rev. Lett. **100** (13), 136406 (2008).

53. H. J. Monkhorst and J. D. Pack, Phys. Rev. B **13** (12), 5188-5192 (1976).

54. R. Hill, Proceedings of the Physical Society. Section A **65** (5), 349-354 (1952).

55. S. P. Lyon and J. D. Johnson, Report No. LA-UR-92-3407, 1992.

56. S. L. Thompson, Report No. SAND89-2951, 1990.

57. R. M. More, K. H. Warren, D. A. Young and G. B. Zimmerman, Phys. Fluids **31** (10), 3059-3078 (1988).

58. D. A. Young and E. M. Corey, J. Appl. Phys. **78** (6), 3748-3755 (1995).

59. G. I. Kanel, W. J. Nellis, A. S. Savinykh, S. V. Razorenov and A. M. Rajendran, J. Appl. Phys. **106** (4), 043524 (2009).